ULTRASONIC IMAGING **33,** 119-133 (2011)

Lesion Detectability in Diagnostic Ultrasound with Short-Lag Spatial Coherence Imaging

JEREMY J. DAHL, DONGWOON HYUN, MUYINATU LEDIJU AND GREGG E. TRAHEY

Department of Biomedical Engineering
Duke University
Durham, NC 27708
Jeremy.dahl@duke.edu

We demonstrate a novel imaging technique, named short-lag spatial coherence (SLSC) imaging, which uses short distance (or lag) values of the coherence function of backscattered ultrasound to create images. Simulations using Field II are used to demonstrate the detection of lesions of varying sizes and contrasts with and without acoustical clutter in the backscattered data. B-mode and SLSC imaging are shown to be nearly equivalent in lesion detection, based on the contrast-to-noise ratio (CNR) of the lesion, in noise-free conditions. The CNR of the SLSC image, however, can be adjusted to achieve an optimal value at the expense of image smoothness and resolution. In the presence of acoustic clutter, SLSC imaging yields significantly higher CNR than B-mode imaging and maintains higher image quality than B-mode with increasing noise. Compression of SLSC images is shown to be required under high-noise conditions but is unnecessary under no- and low-noise conditions. SLSC imaging is applied to *in vivo* imaging of the carotid sheath and demonstrates significant gains in CNR as well as visualization of arterioles in the carotid sheath. SLSC imaging has a potential application to clutter rejection in ultrasonic imaging.

Key Words: Acoustic noise; clutter reduction; spatial coherence; spatial covariance; ultrasound imaging.

1. INTRODUCTION

One of the primary uses of diagnostic ultrasound is the differentiation of diseased tissue from normal or background tissue, often in the form of detecting focal lesions. A seminal paper compares low contrast lesion detectability of human observers to an ideal observer.[1] In this case, the ideal observer makes a decision on the detectability of a lesion based on the threshold of a lesion's signal-to-noise ratio (SNR), which is a parameter dependent on the lesion's size and contrast and on the imaging system's resolution.

In the presence of acoustical or electronic noise, however, the detectability of a lesion decreases. Acoustical noise or interference, which results from reverberation within subcutaneous tissue layers[2] and off-axis scattering, significantly reduces the visibility of lesions and targets by corrupting the signals returning from the target. Few methods have directly targeted image clutter. Harmonic imaging and multiframe filtering methods can reduce clutter resulting from reverberation in subcutaneous tissue layers.[3-5] Phase aberration correction techniques can reduce clutter associated with scattering from side-lobes or off-axis scattering.[3] Multiframe filtering methods directly address image clutter; however, they are limited to clutter derived from reverberation in near-field tissue layers and are dependent on compression or movement of the imaging target in the direction normal to the transducer.[4,5] Har-

0161-7346//11 $18.00

monic imaging and phase-aberration correction, while successful in reducing some clutter, do not directly address the problem of image clutter.

We have recently introduced an ultrasonic imaging technique capable of forming images based on the spatial coherence of the backscattered echoes.[6] This method, called short-lag spatial coherence (SLSC) imaging, has potential applications in clutter rejection in ultrasonic imaging. Other coherence-based imaging metrics include the generalized coherence factor (GCF),[7] the phase coherence factor (PCF)[8] and the sign coherence factor (SCF).[8] The GCF is a coherence metric derived from a ratio of the coherent backscatter sum to the incoherent backscatter sum after high, spatial-frequency components in the backscatter are removed. The primary application for the GCF metric is to process phase-aberrated signals, where strongly-aberrated signals experienced low GCF values and were rejected by weighting them by the GCF metric. The PCF and SCF are metrics derived from the phase of the backscattered signals and are used to weight the B-mode signal in order to reduce side-lobes of the imaging system. The PCF and SCF metrics, however, are not suitable for clutter rejection, as the phase of the signal is easily corrupted in the presence of high acoustical interference. The GCF is better suited than the PCF or SCF methods for clutter rejection due to its filter but is not ideal for clutter rejection because low frequency signal corruption still influences the GCF calculation.

SLSC imaging utilizes local short-lag coherence metrics to directly form images, rather than pixel weightings applied to a B-mode image. This technique offers several potential advantages over B-mode imaging. In the following, we demonstrate the detectability of a wide range of target lesions using the SLSC imaging technique and compare it to conventional ultrasound. In addition, we introduce noise into the channel data and compare the resulting detectability of these lesions as a function of SNR.

2. BACKGROUND

The spatial covariance of backscattered echoes is predicted by the van Cittert-Zernike (VCZ) theorem applied to ultrasonic signals.[9] If observation of the wavefront is restricted to a single wavelength such that the signal mimics a narrowband signal with frequency f, the spatial covariance of an incoherent source at the surface of a transducer can be described as

$$C(x,y) \quad \left| (u,v)H(u,v) \right|^2 \exp \quad j2 \quad \frac{xu \quad uv}{z} \; du\, dv \tag{1}$$

where (x,y) and (u,v) are the spatial dimensions in the aperture and source planes, respectively, (u,v) is the source function, $H(u,v)$ is the lateral transmit beam amplitude and z is the distance between the source and aperture planes. Eq. (1) states that the spatial covariance of the backscattered echoes is the Fourier transform of the square of the product of the transmit beam amplitude and the source function.

Consider a transducer with a receiving aperture of N elements. $s_i(n)$ and $s_j(n)$ are the zero-mean signals received by the ith and jth elements at depth n, in samples, after the elements have been time-delayed to account for geometric path-length differences. The spatial covariance can be estimated between elements i and j by

$$C_{ij} \quad \sum_{n \; n_1}^{n_2} s_i(n) s_j(n) \tag{2}$$

A spatial covariance function can be computed as a function of element separation, or lag $m=j-i$ for the entire aperture by

$$\hat{C}(m) \quad \frac{1}{N \quad m} \sum_{i=1}^{N \quad m} \sum_{n=n_1}^{n_2} s_i(n) s_{i \quad m}(n) \tag{3}$$

By normalizing the spatial covariance function, the influence of the magnitude of the echo is eliminated from the spatial coherence terms. If the spatial covariance function is normalized by the variance of the signals $s_i(n)$ and $s_{i+m}(n)$, the spatial correlation as a function of element lag is produced:

$$\hat{R}(m) \quad \frac{1}{N \quad m} \sum_{i=1}^{N \quad m} \frac{\sum_{n=n_1}^{n_2} s_i(n) s_{i \quad m}(n)}{\sqrt{\sum_{n=n_1}^{n_2} s_i^2(n) \quad \sum_{n=n_1}^{n_2} s_{i \quad m}^2(n)}} \tag{4}$$

The spatial correlation in Eq. (4) is the spatial coherence function that is used to compute the short-lag spatial coherence (SLSC) metric, R_{sl}. As previously demonstrated, the primary differences in coherence for different targets mostly occur in the regions of short lags.[6] Therefore, the SLSC metric is computed at depth n as the integral of the spatial coherence function (Eq. (4)) over the first M lags:

$$R_{sl} \quad \int_{1}^{M} \hat{R}(m)\, dm \quad \sum_{m=1}^{M} \hat{R}(m) \Delta m \tag{5}$$

In this equation, m is typically 1, and, therefore, the SLSC metric is simply the sum of the correlation coefficients over the first M lags. Because the spatial coherence is scaled by the transmit beam, which is itself a function of the transmit aperture, M is best described as a fraction of the transmit aperture. For short lags, M typically encompasses a lag equivalent to 1 to 30% of the transmit aperture. To create SLSC images, the R_{sl} is computed at every pixel. It is important to keep in mind that because of the normalization in Eq. (4), SLSC imaging is fundamentally a nonlinear imaging process in that it is not linearly related to scattering strength.

3. METHODS

A. Lesion simulations

Field II[10,11] was employed to simulate B-mode and SLSC images of lesions of varying size and contrast. For these simulations, a linear 8 MHz transducer array with 60% bandwidth was used to image the lesions. The transducer was focused at 2 cm (F/2) with 50 elements having a pitch of 0.2 mm. All lesions were placed at the focal depth of the transducer.

Thirty-five lesion types were simulated, created from 5 lesion sizes and 7 intrinsic contrasts. The size of the lesions varied from 1 mm to 5 mm diameter in increments of 1 mm, and the intrinsic contrast of the lesions were -40, -20, -12, -6, 6, 12 and 20 dB. The imaging medium and lesions were created by randomly positioning points in 3D Cartesian coordinates with a density of 20 scatterers per resolution volume. The intrinsic contrast of the lesion was adjusted by altering the mean scattering strength of the subresolution scatterers in the lesion volume relative to the scattering strength of the background scatterers. For each of the 35 le-

sion types, four simulations were performed with different random positions and amplitudes of the scatterers.

For each simulation, the radiofrequency (rf) echo signals from each of the 50 elements were acquired. Dynamic receive focusing was applied to channel signals to account for path-length differences. Acoustic noise was added to the channel signals by passing white noise through a bandpass filter with cutoff frequencies equal to the -6 dB bandlimits of the transducer spectrum. The root-mean-square (rms) amplitude of the filtered white noise was adjusted to -40, -20, -12, -6, 0, 6, 12, 20 and 40 dB, relative to the rms amplitude of the background signal.

For each combination of lesion and noise, a B-mode image was constructed by delay-and-sum beamforming the channel signals. SLSC images were created from the same set of channel signals by implementing Eqs. (4) and (5). Unless otherwise noted, the M in Eq. (5) was set to 24% (lag of 12) of the transmit aperture.

B. Lesion detectability

In 1983, Smith et al presented a framework for the detectability of low contrast lesions in medical ultrasound.[1] They derived a threshold for lesion detectability based on a lesion signal-to-noise ratio (SNR) for an ideal observer. This lesion SNR was based on the resolution of the imaging system, the diameter of the lesion, and the contrast-to-noise ratio (C) between the intensities of the lesion and background. Although this detectability metric is quite useful, C is unknown and difficult to determine for other ultrasonic imaging modes, such as SLSC imaging. In addition, because radiologists, sonographers and other ultrasound users typically observe the magnitude of B-mode images, C of the image magnitude is typically the parameter of interest rather than intensity.

In a second publication, Smith and Wagner[12] compared their lesion detectability to a contrast-to-noise ratio (CNR) proposed by Patterson and Foster.[13] The CNR was based on the magnitude of the imaging modality and, for typical B-mode imaging modalities, Smith and Wagner showed that the two detectability metrics were equivalent. Therefore, we employ CNR to determine lesion detectability using the definition proposed by Patterson and Foster:

$$CNR \quad \frac{S_i \quad S_o}{\sqrt{\begin{matrix}2 & 2\\ i & o\end{matrix}}} \tag{6}$$

where S_i and S_o are the spatial means of the image inside and outside the lesion, respectively, and $_i$ and $_o$ are the standard deviations of the image inside and outside the lesion, respectively.

Significance of differences in CNR between B-mode and SLSC imaging was determined using a two-tailed, paired t-test. Significance is described as the probability (p) that the CNR from the B-mode and SLSC imaging are effectively the same.

B. *In vivo* imaging

SLSC imaging was applied to *in vivo* imaging of the carotid sheath of a 57-year old male human to demonstrate the application of SLSC imaging to clinical imaging. Rf echo signals from the individual elements of a VF10-5 linear transducer array (Siemens Medical Solutions USA, Inc., Issaquah, WA) were acquired on a SONOLINE Antares™ scanner (Siemens Medical Solutions USA, Inc.). A custom synthetic aperture method was used to acquire the channel signals through the use of the Axius Direct™ Ultrasound Research Interface (Siemens Medical Solutions USA, Inc.).[14]

The synthetic aperture method is a modified version of the method described by Dahl et al.[15] The synthetic aperture method acquires the individual channel signals by transmitting a pulse from a specified transmit aperture and recording the rf echo on an individual element. The same pulse is transmitted from the same aperture until all echoes on all elements are acquired. The process is then repeated for the next transmit aperture, until the channel signals for all transmit apertures (and thus, image lines) are acquired. Reference signals are acquired every 32 transmit events. These reference signals are conventional imaging lines (delay-and-summed from full transmit and receive apertures) that are used to assess and correct axial motion in the synthetic aperture data.

The rf echo signals from the individual channels were acquired for 54 image lines and two focal depths (1.5 and 2.5 cm). Sixty-four element signals centered around the transmit aperture were acquired for each image line. An F/2 transmit focus with a transmit frequency of 8.9 MHz was used. For comparison, the beamformed rf signals of full B-mode images using the same focal depths were acquired. Following acquisition of the channel signals, the signals were corrected for axial motion using the reference signals described previously. Axial motion was determined by the temporal shift in the maximum of the cross-correlation between reference signals. The axial motion was then linearly upsampled (using the assumption of linear motion between reference signals) by a factor of 33. The upsampled estimate of axial motion was then used to correct the channel signals by shifting the channel signals by the estimated motion.

After correction of axial motion, the channel signals were bandpass filtered. SLSC images were implemented by applying Eqs. (4) and (5) at every pixel. Both B-mode and SLSC images from the two focal depths were combined to create a single image with optimal focusing at 1.5 and 2.5 cm. CNR was calculated on objects in the carotid sheath using Eq. (6).

4. RESULTS

Figure 1 displays matched lesion images using B-mode (left) and SLSC (right) imaging. The B-mode images are log-compressed and show 50 dB of dynamic range, while the SLSC images are not compressed and show a normalized range of 0 to 0.95. For the SLSC images, M is set to 12, which is equivalent to 24% of the transmit aperture. The individual lesion images are spliced together for easier comparison. In these images, three intrinsic contrasts are shown, -40, -12, and 12 dB from left to right and all lesion diameters are shown, increasing from 1 to 5 mm from top to bottom, respectively. The B-mode image shows easily visible lesions, except perhaps at the smallest (1 mm) diameter. Most of these lesions are also easily visible in the SLSC image; however, the characteristics of the lesions change somewhat. The -40 dB lesions are easily visible in both images, although they appear more hypoechoic in the SLSC images. In addition, the 1 mm lesion is slightly more visible, subjectively, in the SLSC image. The -12 dB lesions are well visualized in the B-mode image, with the 1 mm diameter lesion most difficult to visualize. In the SLSC images, these lesions change appearance as the lesion size decreases. In the 4 and 5 mm lesions, the lesions appear to have a darker appearance around the edges of the lesion with the middle of the lesion appearing much brighter. The 3 mm lesion appears slightly different than the 4 and 5 mm lesions in that the lesion has a more uniform appearance inside the lesion. At 1 and 2 mm, the lesions begin to appear more like the -40 dB lesions, having less fill-in.

The positive contrast lesions in SLSC images have markedly different appearance and visibility compared to the B-mode images. Whereas all of the lesions are visible in the B-mode

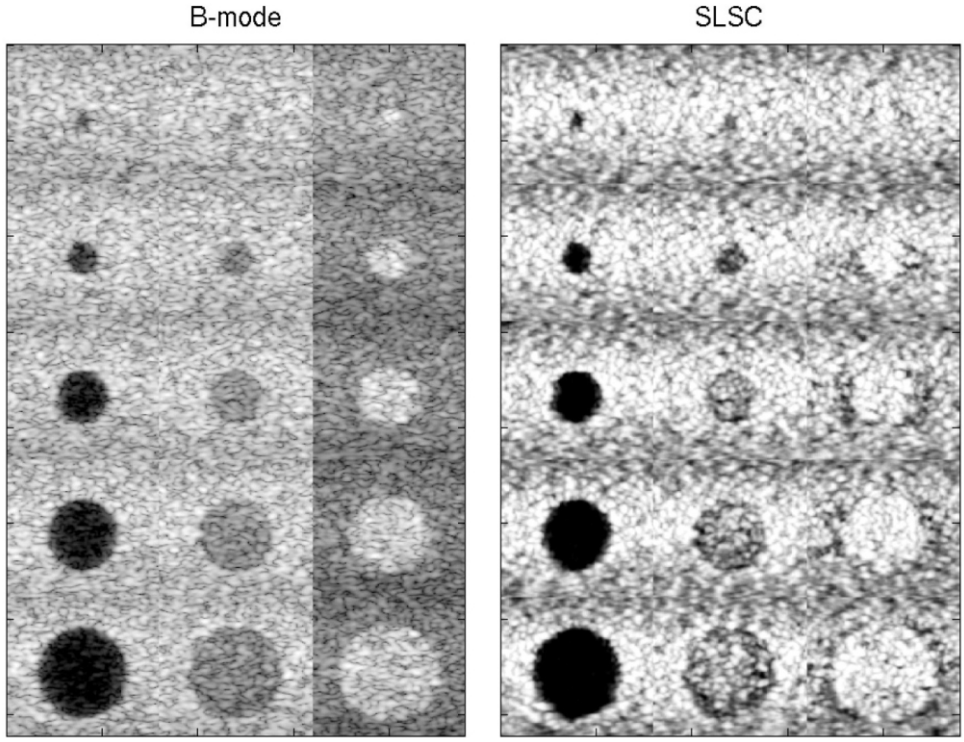

FIG. 1 B-mode (left) and SLSC (right) images (M=12) of lesions of varying diameter and contrast. From top to bottom, the lesion diameter increases from 1 mm to 5 mm. From left to right, the lesion contrast is -40 dB, -12 dB and 12 dB. The B-mode images are log-compressed and shown with 50 dB of dynamic range and the SLSC images are not compressed and shown with a normalized range of 0 to 0.95.

images, only the larger size lesions are easily visible in the SLSC image. In addition, the 2 to 5 mm lesions have a dark halo on the lateral sides of the lesion. The 1 mm lesion is nearly indistinguishable from the background.

Figure 2 displays the average CNR from four realizations of each lesion as a function of diameter and intrinsic contrast for both the B-mode and SLSC images. The graph in figure 2 is capped at 3.1 in order to display, in greater detail, the CNR values for the lesions with lower intrinsic contrast (in our experience, lesions having CNR values greater than 3.1 are easily distinguishable from the background). For the SLSC images, M is set to 12 (24% of the aperture). The error bars in this graph indicate one standard deviation. At the high negative contrasts (-40 and -20 dB), SLSC imaging yields significantly greater CNR. At low contrasts, SLSC imaging is shown to be equivalent, or sometimes worse, than B-mode imaging. For the positive contrast lesions, SLSC imaging is significantly worse at 6 and 12 dB intrinsic contrast and does not do better than B-mode imaging until the contrast is increased to 20 dB.

Figure 3 shows the CNR of the lesions as a function of M for four intrinsic contrasts (-40, -12, 12 and 20 dB) and averaged over four simulations. Error bars indicating one standard deviation are displayed in 3(a) to show the extent of the variation in measurements, although they are omitted in figures 3(b)–3(d) for clarity. The CNR for the comparative lesions in the B-mode images are placed on the left of the graphs at the abscissa labeled 'B'. At -40 dB, the CNR changes most dramatically as a function of diameter and intrinsic contrast. At large contrast (positive or negative), an optimal CNR is observed for each of the lesions. As the intrinsic contrast decreases (either positive or negative), the peak in CNR shifts toward lower

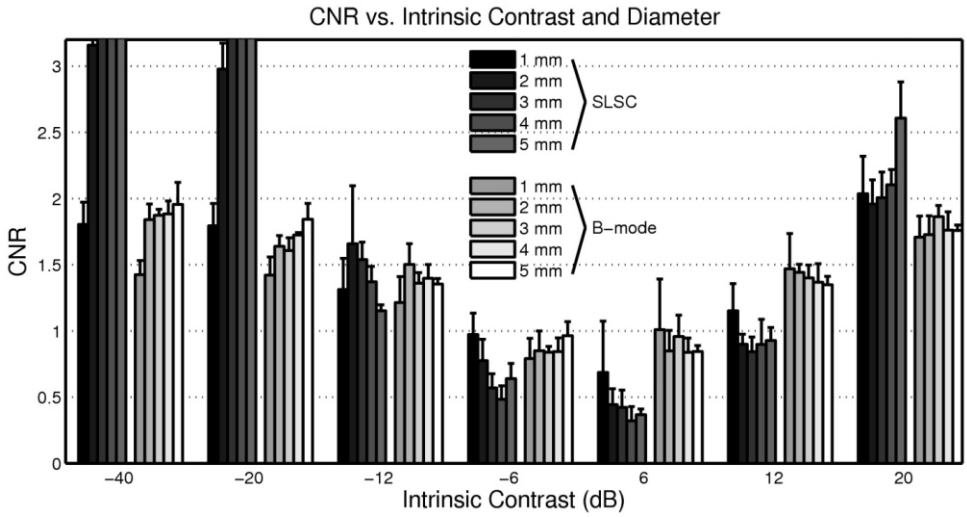

FIG. 2 Average CNR of the lesions, from four simulations, as a function of intrinsic contrast and diameter from B-mode and SLSC (M=12) images. Error bars indicate one standard deviation of the CNR from the four simulations.

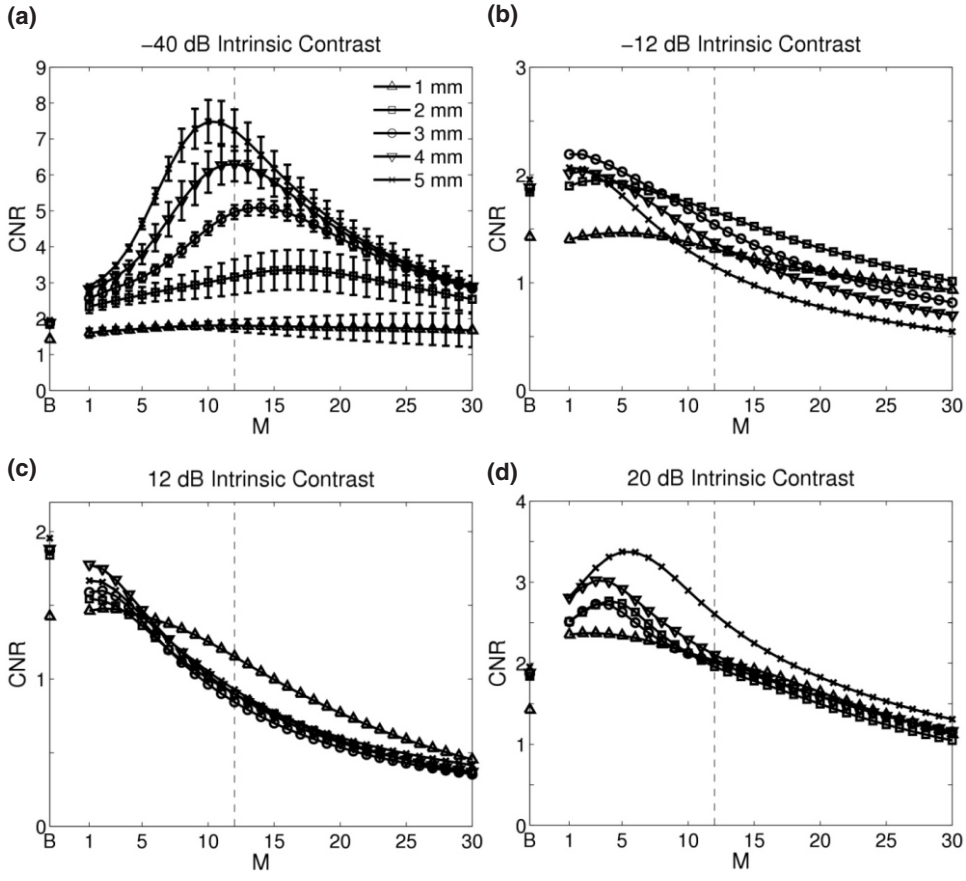

FIG. 3 CNR as a function of M and lesion diameter for lesion contrasts of (a) -40 dB, (b) -12 dB, (c) 12 dB and (d) 20 dB. The CNR values described by the abscissa labeled 'B' on the far left of the axis indicate the CNR for the lesions in the comparative B-mode images. The dotted line at M=12 indicates where CNR was measured in figure 2. Error bars in (a) indicated one standard deviation, although error bars are omitted in (b)–(d) for clarity.

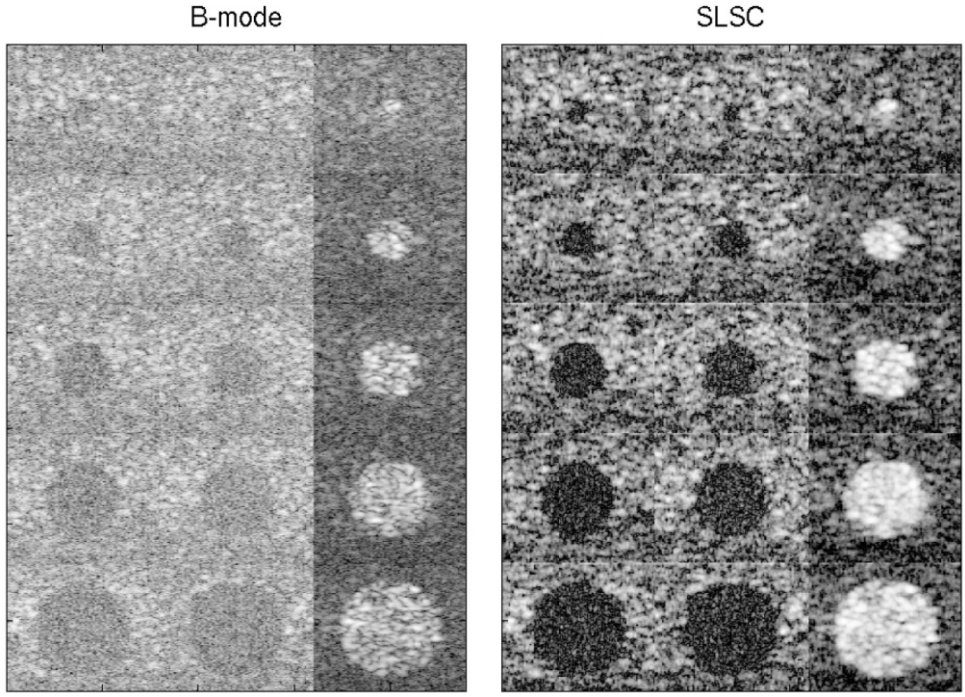

FIG. 4 B-mode (left) and compressed SLSC (right) images of lesions of varying diameter and intrinsic contrast with noise added to the channel signals. The SNR of the channel signals is -12 dB, giving the summed rf signals an SNR of 5 dB. The lesion diameters and intrinsic contrasts are identical to those of figure 1.

M, as demonstrated by figures 3(b) and 3(c). The dotted lines in these graphs indicate where CNR was measured for figure 2.

Figure 4 shows images of the same lesions depicted in figure 1, except that 12 dB noise has been added to the channel signals. Because the noise is uncorrelated over the 50 elements of the simulated transducer, the delay-and-sum beamformed noise is effectively reduced by a factor of $\sqrt{50}$, giving the images an SNR of 5 dB in the B-mode images. Both the B-mode and SLSC images are log-compressed and show 50 dB of dynamic range.

The negative contrast lesions are difficult to distinguish in the B-mode images, although they are easier to distinguish at the larger diameters. The positive contrast lesions are easily distinguished because the noise is relative to the background signal strength and thus, the signals originating from the positive contrast lesions have an SNR of approximately 0 dB (or 17 dB in the B-mode image). The -40 and -12 dB lesions in the B-mode images appear indistinguishable from each other.

The lesions in the SLSC image are better visualized than in the B-mode images, although like the B-mode images, the -40 and -12 dB lesions are indistinguishable from each other. The positive contrast lesions are well visualized in this case, compared to figure 1, and no dark rings or halos appear in the image. The 1 mm lesion is much more visible in the SLSC image than in the B-mode image.

The CNR measured over four simulations for the lesions with -12 dB of channel noise is shown in figure 5 as a function of diameter and intrinsic contrast. Aside from the changes in CNR due to the addition of noise, there is a change in the relative performance between B-mode and SLSC imaging as compared to figure 2. Previously, SLSC imaging only outperformed B-mode imaging in CNR for high-contrast lesions. In the presence of high-amplitude noise, SLSC imaging now outperforms B-mode imaging at all contrasts and diameters ($p < 0.005$ for all contrasts and diameters).

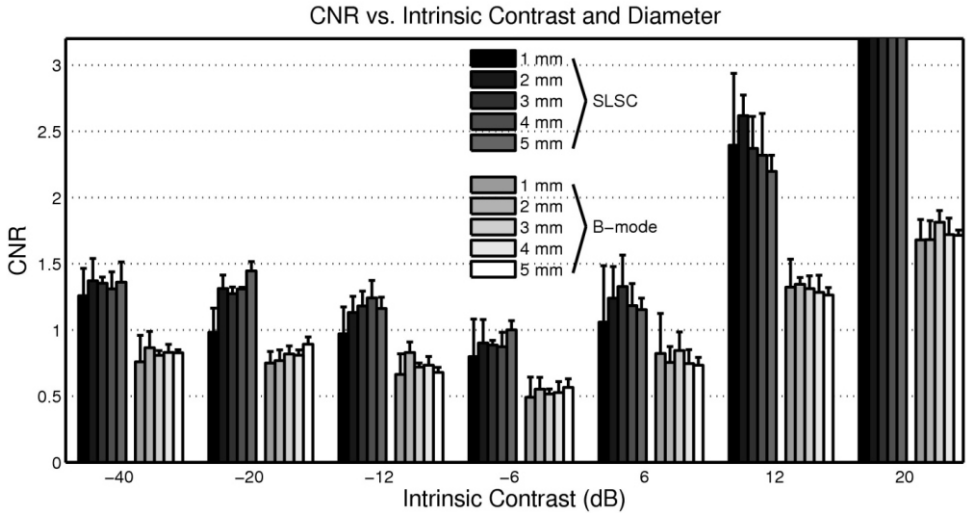

FIG. 5 Average lesion CNR in the B-mode and SLSC (M=12) images over four simulations as a function of intrinsic contrast and diameter with 12 dB of noise added to the channel signals. Error bars indicate one standard deviation.

The CNR as a function of channel noise is shown in figure 6 for a 3 mm diameter lesion at -40, -12 and 20 dB intrinsic contrasts. SLSC imaging consistently shows higher CNR at all but the lowest SNR values, in which the CNRs of SLSC and B-mode imaging are approximately the same. The CNRs for the B-mode images show a similar roll-off as a function of noise for both the low- and high-contrast lesions. The CNRs for the -40 and -12 dB lesions maintain a constant value down to 0 dB SNR, at which point the CNRs roll off toward zero. In SLSC imaging, the high-negative-contrast lesions show a different result compared to low negative-contrast lesions. For high negative-contrast lesions, the CNR is relatively constant down to an SNR of 6 to 10 dB, at which point it begins to roll off toward zero. For low-contrast lesions, the CNR is initially flat down to approximately 20 dB SNR, at which point it increases and peaks around 6 to 10 dB and then rolls off toward zero.

In the high positive-contrast case, there is a peak in the CNR as a function of SNR for the SLSC images. At the high SNR values, the CNR in the SLSC images is relatively close to the B-mode value. As SNR decreases, the CNR ramps up and peaks at approximately -12 dB. This peak occurs at a lower SNR value than the low-negative-contrast-lesions. In addition, the B-mode image displays a roll-off at a lower SNR than the negative-contrast lesions.

The speckle SNR (i.e., the ratio of the mean of the background image to its standard deviation) as a function of channel noise is shown in figure 6(d). As expected, the speckle SNR of the B-mode image remains constant at 1.91, even as the noise dominates the image. The speckle SNR in the SLSC images varies as a function of noise. The speckle SNR is significantly higher, indicating a much smoother background, at channel SNRs down to -6 dB, at which point both imaging modes are equivalent. As the noise dominates in the SLSC image, the speckle SNR goes to zero.

Figure 7 demonstrates B-mode, compressed SLSC and uncompressed SLSC images of a 3 mm diameter, -12 dB contrast lesion as a function of increasing noise. In each of the three modes, the images, from left to right, have increasing noise with SNR values equal to the points depicted in figure 6. As the noise increases, the visibility of the lesions becomes worse. It is apparent, however, that the SLSC images yield better visualization of the lesions at some of the higher noise strengths. The compressed SLSC images show better visualization of the lesions at high noise strengths than the uncompressed SLSC images, while the uncompressed SLSC images show better visualization of the lesions at low noise strengths than the compressed SLSC images.

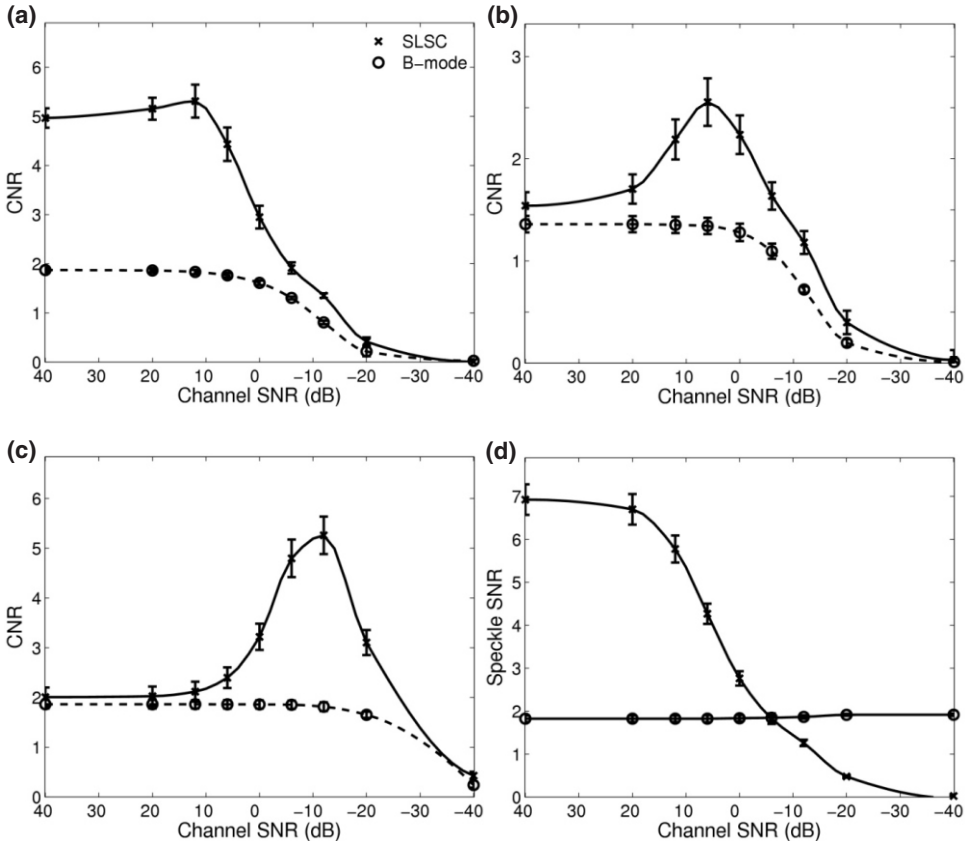

FIG. 6 Average CNR of a 3 mm diameter lesion with (a) -40 dB, (b) -12 dB and (c) 20 dB intrinsic contrast as a function of channel noise. (d) Average speckle SNR of the B-mode and SLSC images as a function of channel noise. Error bars indicate one standard deviation of the measurement from four simulations. For the SLSC images, M=12.

Figure 8 demonstrates the application of SLSC imaging to *in vivo* imaging of the human carotid sheath. The jugular vein (JV) and vagus nerve (VN) are indicated in the B-mode image. The B-mode image shows 45 dB of dynamic range. This dynamic range was chosen to eliminate as much clutter as possible without significantly diminishing diagnostically useful information. The CNRs of the arterioles (as indicated by the arrows in figure 8(b)) in the B-mode image, starting on the left and moving clockwise, are 0.88, 0.35, 1.14, 1.57 and 0.99, respectively.

In the SLSC image (Fig. 8(b)), the arterioles become well visualized. The arterioles are indicated by arrows and are much better visualized in the SLSC image compared to the B-mode image. In addition, the upper boundary of the carotid artery is better defined due to the reduction in clutter. The CNRs of the arterioles in the SLSC image, starting on the left and moving clockwise, are 1.91, 1.61, 2.55, 2.92 and 2.81, respectively.

5. DISCUSSION

Because SLSC imaging is based on the coherence of the backscattered signal, it is a nonlinear imaging method in terms of its relationship to target backscatter magnitude and there-

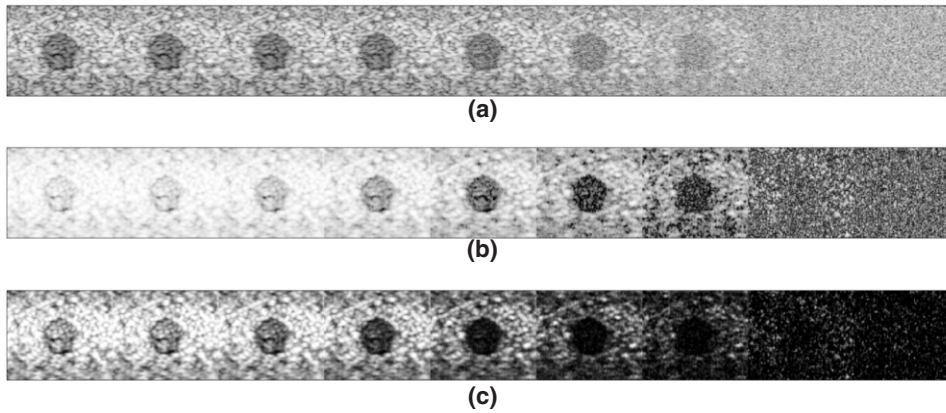

FIG. 7 (a) B-mode, (b) compressed SLSC and (c) uncompressed SLSC images of the 3 mm diameter, -12 dB contrast lesions. Increasing noise (decreasing SNR) appears from left to right across the images.

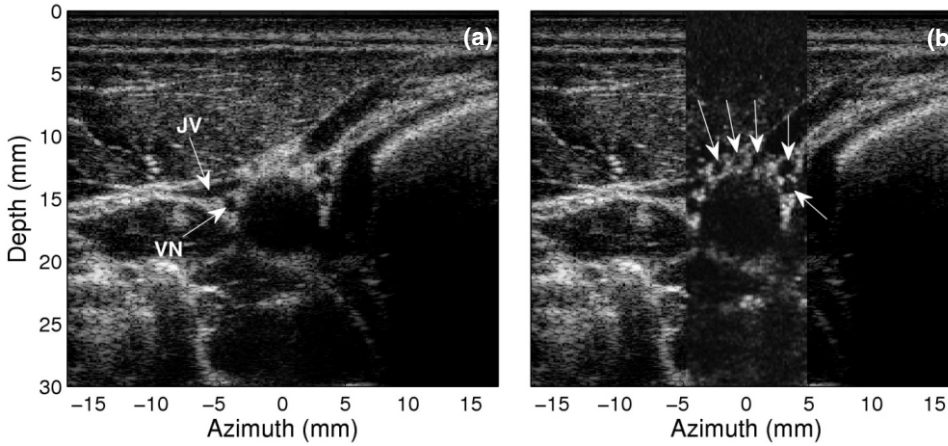

FIG. 8 (a) B-mode and (b) SLSC images of a transverse view of the carotid sheath. In (b), the SLSC image is overlayed on top of the B-mode image. Demonstrated are the vagus nerve (VN), jugular vein (JV), and several arterioles (arrows) that surround the common carotid artery. Note that the majority of the arterioles are not well visualized in the B-mode image due to clutter. The B-mode image is displayed with 45 dB of dynamic range, while the SLSC image is not compressed.

fore produces some characteristic effects. The normalization of the coherence function in Eq. (4) effectively removes brightness as a contributing factor to the image. Thus, objects of different intrinsic contrast would be expected to have the same brightness in the SLSC image because they would have the same spatial-coherence values. However, as observed in figures 1 and 2, the lesions are differentiated from the background as well as or better than B-mode imaging, with few exceptions. As indicated by figure 3 and discussed by Lediju et al,[6] these exceptions may be improved upon by choosing the optimal M for the SLSC image. The value of M, however, will affect image resolution and the smoothness of the background.[6]

In B-mode images, all scatterers within the hourglass-shaped isochronous volume contribute to the echo magnitude displayed at any given point. However, for SLSC imaging, off-axis scatterers suppress spatial coherence while on-axis scatterers reinforce coherence. The suppression of coherence by off-axis scatterers is scaled by the echo intensity of both on- and off-axis scatterers and by their lateral distance from the beam axis.

Therefore, for small negative intrinsic-contrast lesions, the low brightness inside the lesion in the SLSC image is generated by echo interference from the off-axis background scatterers, which suppress coherence. For large negative intrinsic-contrast lesions, a dark halo appears around the edges of the lesion, which is more prominent at the lateral borders of the lesion. At the borders, the off-axis interference has greater amplitude than in the center of the lesion, making this area appear darker. In the center of the lesion, the scattering from off-axis is weaker and has less effect on the on-axis signal and therefore, the brightness in the center of the lesion is closer to the background brightness.

For positive intrinsic-contrast lesions, the high-amplitude signals of the lesion generate high-amplitude off-axis scattering in the background, which creates a dark halo at the lateral borders of the positive-contrast lesions. Some visibility of the axial borders occurs due to the curved surface of the lesion; however, there is less of a halo at the axial borders because the off-axis scattering is much weaker relative to the on-axis signal.

The target lesions in figure 1 are adequately visible in the B-mode and SLSC images. The primary advantage of SLSC imaging, however, is in clutter reduction. Figure 4 displays the same lesions with acoustical noise (shaped by the passband of the transducer) and demonstrates the ability of SLSC imaging to generate better lesion detectability than B-mode imaging under high-amplitude clutter.

B-mode imaging reduces uncorrelated acoustic noise using the delay-and-sum beamforming process. Uncorrelated noise in the backscattered signals will decrease with $\sqrt{N}$, where N is the number of elements in the receive array. If the clutter or noise is sufficiently strong, the backscattered signal is essentially overwritten and the delay-and-sum beamformer is unable to generate a high-quality image. This is apparent in the B-mode images where the -40 and -12 dB lesions look identical under extreme acoustical interference.

In SLSC imaging, pixel brightness values depend entirely on the coherence of the backscatter. Therefore, uncorrelated acoustic noise generates very low values in SLSC imaging. Under the case of high-amplitude acoustical interference where the signal is essentially destroyed, SLSC imaging yields the same result as uncorrelated acoustic noise. This is similar to the case of B-mode imaging and can be seen in the SLSC images of the -40 and -12 dB lesions in figure 4 where the two lesions appear nearly identical. SLSC imaging is less sensitive to the effects of noise, however, than B-mode imaging. As demonstrated by the CNR values in figures 5 and 6, SLSC imaging yields better lesion detectability in all cases in the presence of noise.

The most relevant cases in lesion detectability with SLSC imaging are when the CNR values in the B-mode images are low (CNR < 1). Although the threshold for detection depends on both lesion size and intrinsic contrast,[1] this threshold is often in the region of a CNR of 1. The CNRs of the low intrinsic contrast lesions (Fig. 5) and arterioles surrounding the carotid artery (Fig. 8) in the B-mode images indicate that they would be very difficult to detect. However, SLSC imaging demonstrates an increase in CNR such that the lesion (or arteriole) reaches a much more detectable level. SLSC imaging demonstrated an increase in CNR of approximately 0.4–0.5 in the lesion simulations but larger than 1 in the *in vivo* images of the arterioles.

The CNR of the positive-contrast lesions in figure 5 demonstrate much higher values than the CNR in the noise-free SLSC images (Fig. 2). This occurs because the strength of the acoustical noise is applied relative to the background signal, so the positive contrast lesions maintain much higher SNR than the surrounding background. Thus, the background values are decreased relative to figure 1 and the signal from the positive-contrast lesions remains relatively unaffected. This increases the CNR of these lesions considerably, as demonstrated in figure 6(d) at the lower SNR values. Comparatively, the CNR of the lesions in the B-mode image decrease slightly relative to the noise-free case, as would be expected.

For the high-negative intrinsic-contrast lesions, the CNR in the SLSC image remains constant as a function of channel SNR before rolling off toward zero at the 6-10 dB mark (Fig. 6). The CNR maintained by the SLSC image is much larger than the B-mode image and maintains higher values as the SNR decreases. The low-negative intrinsic-contrast lesions produce a distinct peak in CNR around the 6-10 dB SNR mark. As the noise begins to dominate the signal in the low-contrast region of the lesion, the SLSC value in that region decreases whereas the signal in the background maintains coherence and is less affected. Therefore, the CNR continues to increase until the noise impacts the background signal, at which point the entire image begins to degrade. This is contrary to the case of B-mode images, which decrease in quality as the noise increases. In the case of the positive intrinsic-contrast lesion (Fig. 6(c)), the curve in figure 6(b) is effectively shifted to the right because the noise decreases the values in the background but not within the lesion. Thus, the SLSC CNR does not begin to decrease until the channel noise begins to affect the signal resulting from the positive-contrast lesion. For comparison, the SNR of channel signals has previously been measured in human breast, liver, and thyroid[15] and was determined to be in the range of approximately 3–13 dB. These numbers, however, are specific to the imaging system used and the body *habitus* of the patient. Actual SNR values of channel signals could potentially be lower in patients that are overweight or obese.

The speckle SNR (Fig. 6(d)) for SLSC imaging has significantly higher values than for B-mode imaging at low to mid ranges of channel noise. This indicates a much smoother background in SLSC imaging, much like that obtained by spatial compounding, a common speckle-reduction technique used in B-mode imaging. The difference, however, is that spatial compounding is often implemented with some form of tradeoff in either frame rate or resolution. In SLSC imaging, speckle and clutter reduction are obtained without the loss in frame rate or resolution. As the channel noise continues to increase, the speckle SNR goes to zero. This is unlike conventional B-mode imaging, where the resulting SNR is 1.91 regardless of the strength of the channel noise.

As the background signal begins to deteriorate from the noise in the SLSC image, it becomes more advantageous to use compression on the image to better visualize the lesion. Figure 7 demonstrates the comparison of SLSC imaging with and without compression. At the low-noise levels, the compressed image becomes saturated and visualization of the lesion is poor, whereas in the uncompressed images, visualization of the lesion is good. As the noise increases, the uncompressed image begins to darken and the few coherent ‘speckle’ spots create a high dynamic range, much like B-mode imaging. Thus, compression of these images demonstrates much better visualization of the lesions (the fifth and sixth lesions from the left, for example). As the noise dominates the background signal, however, no lesions are visible in either the B-mode or SLSC images.

Figure 8 shows a demonstration of the capabilities of SLSC imaging in clinical imaging situations. Although some of the arterioles are visible in the B-mode image, the SLSC image reveals all arterioles and, at the same time, shows clear definition of the location and boundaries of each of them. The primary application of SLSC imaging would be in clutter reduction, where SLSC imaging could potentially play a complementary imaging role to conventional B-mode imaging.

6. CONCLUSIONS

We have demonstrated a novel imaging technique (SLSC imaging) based on the spatial coherence of the backscattered field of ultrasound. Lesion detectability with SLSC imaging was demonstrated to be as good as B-mode imaging in most cases under noise free condi-

tions. In the presence of noise, however, SLSC imaging significantly improved lesion detectability, as measured by the lesion's CNR. In the presence of high acoustical interference, both B-mode and SLSC imaging lost integrity in imaging low-scattering-amplitude regions, thus making lesions with different intrinsic contrast appear identical. However, SLSC imaging yielded superior lesion detectability in these high-noise images. SLSC was applied to *in vivo* imaging of the carotid sheath and showed improved visualization of arterioles that were obscured by clutter.

SLSC is a nonlinear imaging technique. Therefore, the performance of the system does not follow typical linear responses of systems to various imaging conditions, including noise. SLSC imaging demonstrated different responses for different lesion sizes and intrinsic contrasts, as well as nonlinear behavior as a function of noise. The success of SLSC imaging will depend on the significance of the nonlinear behaviors and the degree to which these nonlinear behaviors can be tolerated.

ACKNOWLEDGMENTS

This work was supported by NIH grants R21-EB008481 from the National Institute of Biomedical Imaging and Bioengineering and R01-CA114093-04S1 from the National Cancer Institute. The authors wish to thank the Ultrasound Division at Siemens Medical Solutions USA, Inc. for their in-kind and technical support.

REFERENCES

1. Smith SW, Wagner RF, Sandrik JM, Lopez H. Low contrast detectability and contrast/detail analysis in medical ultrasound, *IEEE Trans Sonics Ultrason 30*, 164–173 (1983).

2. Dahl JJ. Impact of the structure of subcutaneous tissue on ultrasonic clutter, in *Proc IEEE Ultrason Symp* (2010).

3. Pinton GF, Trahey GE, Dahl JJ. Sources of image degradation in fundamental and harmonic ultrasound imaging: a nonlinear fullwave simulation study, *IEEE Trans Ultrason Ferroelect Freq Contr 58*, 754–765 (2011).

4. Lediju M, Pihl MJ, Hsu SJ, et al. A motion-based approach to abdominal clutter rejection, *IEEE Trans Ultrason Ferroelect Freq Contr 56*, 2437–2449 (2009).

5. Mauldin FW, Jr., Lin D, Hossack JA. A singular value filter for rejection of stationary artifact in medical ultrasound, in *Proc IEEE Ultrason Symp* (2010).

6. Lediju M, Trahey GE, Byram BC, Dahl JJ. Short-lag spatial coherence of backscattered echoes: imaging characteristics, *IEEE Trans Ultrason Ferroelect Freq Contr* (2011, in press).

7. Li PC, Li ML. Adaptive imaging using the generalized coherence factor, *IEEE Trans Ultrason Ferroelect Freq Contr 50*, 128–141 (2003).

8. Camacho J, Parrilla M, Fritsch C. Phase coherence imaging, *IEEE Trans Ultrason Ferroelect Freq Contr 56*, 958–974 (2009).

9. Mallart R, Fink M. The van Cittert-Zernike theorem in pulse echo measurements, *J Acoust Soc Am 90*, 2718–2727 (1991).

10. Jensen JA. Field: A program for simulating ultrasound systems, *Med Biol Eng Comp, col. 10th Nordic-Baltic Conference on Biomedical Imaging 4*, 351–353 (1996).

11. Jensen JA, Svendsen NB. Calculation of pressure fields from arbitrarily shaped, apodized, and excited ultrasound transducers, *IEEE Trans Ultrason Ferroelect Freq Contr 39*, 262–267 (1992).

12. Smith SW, Wagner RF. Ultrasound speckle size and lesion signal to noise ratio: verification of theory, *Ultrasonic Imaging 6*, 174–180 (1984).

13. Patterson MS, Foster FS. The improvement and quantitative assessment of b-mode images produced by an annular array/cone hybrid, *Ultrasonic Imaging 5*, 195–213 (1983).

14. Brunke SS, Insana MF, Dahl JJ, et al. An ultrasound research interface for a clinical system, *IEEE Trans Ultrason Ferroelect Freq Contr 54*, 198–210 (2007).

15. Dahl JJ, Soo MS, Trahey GE. Spatial and temporal aberrator stability for real-time adaptive imaging, *IEEE Trans Ultrason Ferroelect Freq Contr 52*, 1504–1517 (2005).